




# Facile synthesis of flower-like CQDs/S-Bi<sub>4</sub>O<sub>5</sub>Br<sub>2</sub> composites as a highly efficient visible-light response photocatalyst for ciprofloxacin degradation

Peijie Weng<sup>1</sup>, Qing Cai<sup>1</sup>, Huadong Wu<sup>1</sup>, Linfeng Zhang<sup>1,3,\*</sup> , Kun Wu<sup>1,2</sup>, and Jia Guo<sup>1,\*</sup>

<sup>1</sup>Key Laboratory for Green Chemical Process of Ministry of Education, Hubei Key Laboratory of Novel Reactor and Green Chemical Technology, School of Chemical Engineering and Pharmacy, Wuhan Institute of Technology, Wuhan 430205, People's Republic of China

<sup>2</sup>The College of Post and Telecommunication of Wuhan Institute of Technology, Wuhan 430073, People's Republic of China

<sup>3</sup>School of Chemical Engineering and Technology, Tianjin University, Tianjin 300072, People's Republic of China

Received: 15 July 2021

Accepted: 25 October 2021

Published online:

3 January 2022

© The Author(s), under exclusive licence to Springer Science+Business Media, LLC, part of Springer Nature 2021

## ABSTRACT

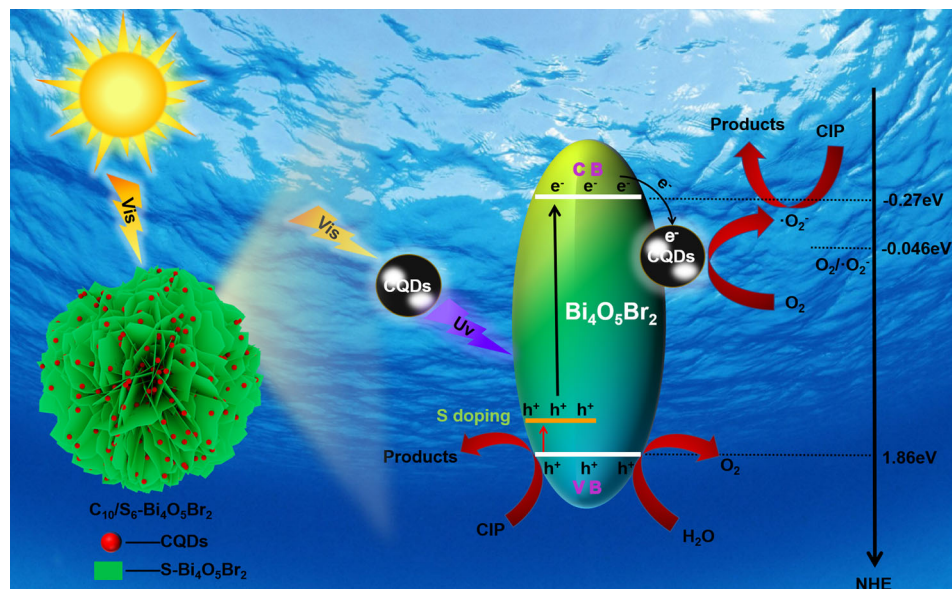
The flower-like CQDs/S-Bi<sub>4</sub>O<sub>5</sub>Br<sub>2</sub> composites photocatalyst with high visible-light response is prepared by adjusting bismuth-rich, S-doped, and introducing carbon quantum dots (CQDs) into the bismuth oxybromide (BiOBr). Particularly, the prepared C<sub>10</sub>/S<sub>6</sub>-Bi<sub>4</sub>O<sub>5</sub>Br<sub>2</sub> composite shows the highest degradation efficiency for the ciprofloxacin (CIP) under visible-light irradiation with the apparent rate constants  $k$  of 0.03798 min<sup>-1</sup>, which is 26.3 times and 10.1 times higher than that of BiOBr and Bi<sub>4</sub>O<sub>5</sub>Br<sub>2</sub>, respectively. The sulfur doping leads to the increase of the specific surface area and decreases of the band gap but retains the original flower-like morphology of Bi<sub>4</sub>O<sub>5</sub>Br<sub>2</sub>. Compared to the pure Bi<sub>4</sub>O<sub>5</sub>Br<sub>2</sub>, CQDs/Bi<sub>4</sub>O<sub>5</sub>Br<sub>2</sub>, and S-Bi<sub>4</sub>O<sub>5</sub>Br<sub>2</sub>, the CQDs introduction and S-doping can improve both of the light absorption range and intensity, as well as the charge transfer efficiency for the C<sub>10</sub>/S<sub>6</sub>-Bi<sub>4</sub>O<sub>5</sub>Br<sub>2</sub> composites. Furthermore, because of the combination of the CQDs and S doped for the Bi<sub>4</sub>O<sub>5</sub>Br<sub>2</sub> composites, the separation efficiency of photo-generated carriers is improved with the recombination rate greatly reduced.

Handling Editor: Joshua Tong.

Address correspondence to E-mail: lfzhang@wit.edu.cn; guojia@wit.edu.cn

<https://doi.org/10.1007/s10853-021-06661-z>

## GRAPHICAL ABSTRACT



## Introduction

In the twenty-first century, an increasing number of people are concerned about these two main challenges: environmental pollution and energy crisis [1]. Recently, many new methods and strategies have been proposed and reported to solve these challenges [2]. There is no doubt that photocatalytic technology may be an ideal method to deal with the above-mentioned challenges due to its green and efficient features, which will have a powerful influence on environmental protection [3, 4]. However, the rational design and preparation of highly efficient photocatalyst is a major difficulty in the realization of this technology [5]. In the reported studies, the prepared photocatalysts just can only be excited by the ultraviolet light, while the sunlight mainly consists of the visible light and infrared light [6]. Therefore, it remains a big challenge to design and explore an ideal photocatalysts to effectively utilize the visible light [7].

Bismuth oxyhalide (BiOX), as a new layered semiconductor photocatalytic material, has attracted more and more attentions because of its good light

absorption and easily controlled band electronic structure [8]. The crystal of the BiOX is a layered structure formed by the interweaving  $[Bi_2O_2]^{2+}$  layers and double slabs of halogen ion layers. Due to the interaction between the atoms in the layer, bismuth oxyhalide materials show good anisotropy in optical and electrical aspects. Therefore, it has been widely applied in the photocatalytic degradation of different pollutants in the environment, hydrogen production by decomposing water, nitrogen fixation,  $CO_2$  conversion, etc. [9–12]. However, the monomer bismuth oxyhalide phase materials still have many shortcomings and these drawbacks may lead to low light absorption capacity, which hinders its further application in photocatalysis. At present, the effective and popular ways to enhance the photocatalytic performances of the bismuth oxyhalide materials mainly include morphology control, element doping, bismuth-rich strategy, semiconductor recombination and defect engineering, etc. [13–17]. Recently, the bismuth-rich bismuth oxybromides have been widely concerned, such as  $Bi_5O_7Br$  [18],  $Bi_3O_4Br$  [19], and  $Bi_4O_5Br_2$  [20]. Many research work have found that the bismuth-rich strategies can effectively regulate the band structure of bismuth oxyhalides and then

improve the photoresponse performance [21]. Accordingly the photocatalytic performances of the BiOBr are greatly improved [22]. Besides the bismuth-rich strategies, the internal structure, the morphology of the BiOBr semiconductor also shows a great influence on its performance [23]. Three-dimensional (3D) flower-like structures constructed at the nanometer scale have shown the advantages of abundant active sites and well stability [24]. Therefore, the photocatalysts with a three-dimensional flower-like structure are expected to show better photocatalytic performance [25]. In addition, element doping is also an important means to improve photocatalytic performance [26]. Relatively speaking, element doping has been widely used as a simple and effective method for the nanomaterials modification [27]. Among these, the non-metal (N, C, P, S, etc.) doping can reduce the band gap of the composites and increase the utilization of visible light [28]. Furthermore, these doped heteroatoms can be obtained by cheap and environmentally friendly hydrothermal or solvothermal methods [29]. Jiang et al. prepared bismuth oxybromide doped with nitrogen or sulfur with urea or thiourea as doping source, and the obtained composite showed high photocatalytic activity and well durability [30].

Recently, carbon quantum dots (CQDs) have been widely used because of their many attractive characteristics, such as abundant earth resources, green environmental protection, and low cost [31]. These carbon-containing materials can expand the use range of light through the up-conversion effect [32]. Many studies have shown that the CQDs can transfer electrons and promote charge separation [33]. In addition, it is reported that carbon quantum dots show up-conversion luminescence, which can effectively utilize sunlight [34]. With the carbon quantum dots, light with a large wavelength can convert into another one with a small wavelength [35]. Because of these outstanding characteristics, CQDs are considered to be excellent co-catalysts for the improvement of photocatalytic activity of semiconductor composites. Therefore, the CQDs have been added into many semiconductors for the photocatalytic performance improvement, such as CQDs/BiOBr [36], CQDs/C<sub>3</sub>N<sub>4</sub> [37], and CQDs/Bi<sub>2</sub>WO<sub>6</sub> [38], etc.

Based on the above considerations, a series of bismuth-rich 3D flower-like Bi<sub>4</sub>O<sub>5</sub>Br<sub>2</sub> composites are designed and prepared through a one-step in-situ reaction process, in which the sulfur is doped and the

CQDs is introduced as the charge mediator and visible light converter. The obtained CQDs/S-Bi<sub>4</sub>O<sub>5</sub>Br<sub>2</sub> composites are carefully studied through physical and chemical characterizations, as well as the DFT calculations. The CQDs/S-Bi<sub>4</sub>O<sub>5</sub>Br<sub>2</sub> composites exhibit heavily enhancement of the photocatalytic degradation efficiency and well stability for different kinds of pollutants. Furthermore, the active components of the CQDs/S-Bi<sub>4</sub>O<sub>5</sub>Br<sub>2</sub> composites are discussed and confirmed based on the ESR characterization and free radical trapping experiments. It is believed that this work will provide an innovative view for constructing 3D flower-like bismuth-rich BiOX composites for environmental remediation.

## Experimental

### Materials

Ciprofloxacin (CIP), Ofloxacin (OFLX) and Tetracycline (TC) were purchased from the Aladdin Chemical Co., Ltd. Other reagents are purchased from the Sinopharm Chemical Reagent Co., Ltd. All of the reagents are used directly without purification.

### Sample preparation and characterization

The Carbon Quantum dots were synthesized by hydrothermal synthesis of citric acid and ethylenediamine. And the Bi<sub>4</sub>O<sub>5</sub>Br<sub>2</sub> was prepared through a solvothermal method according to the reference with minor modification [15]. Lastly, the 0D-CQDs were composited onto the S-doped flower-like Bi<sub>4</sub>O<sub>5</sub>Br<sub>2</sub> microspheres through a one-step in-situ reaction process. In the supporting information part, the sample preparation process, characterization, and DFT calculation of the flower-like CQDs/S-Bi<sub>4</sub>O<sub>5</sub>Br<sub>2</sub> composites are detailed described. And the preparation process of flower-like C<sub>y</sub>/S<sub>x</sub>-Bi<sub>4</sub>O<sub>5</sub>Br<sub>2</sub> composites is depicted in Fig. S1.

### Photocatalytic performance evaluation

The photocatalytic performances evaluation was conducted in a quartz reactor with a 300 W xenon lamp (PLS-SXE300) as the visible light source. Generally, 40 mg of prepared samples is dispersed in 200 mL of CIP solution. After the adsorption-

desorption equilibrium was achieved, then the illumination experiment was started. At a specific sampling time point, 4 mL of the solution was collected, filtered and then measured the absorbance at the characteristic absorption peak to calculate the CIP concentration. The cycles tests are conducted in detail as: the remaining solution was filtered and washed through a 0.22  $\mu\text{m}$  filter membrane, and then dried in an oven at 60  $^{\circ}\text{C}$  for 6 h to obtain the recovered catalyst. Then, the second round of photocatalytic performance was carried out with the recovered catalyst under the same reaction condition. Totally, the above experimental process was repeat for five time for investigating the stability of the prepared CQDs/ $S\text{-Bi}_4\text{O}_5\text{Br}_2$  photocatalyst.

## Results and discussion

### Morphology and microstructure

The crystal structure of the samples are evaluated by XRD (Fig. 1). Firstly, the crystal phases of  $\text{Bi}_4\text{O}_5\text{Br}_2$  (JCPDS: 37-0699) and  $\text{BiOBr}$  (JCPDS: 09-0393) samples are confirmed by XRD characterization. The main diffraction peaks of flower-like CQDs/ $S\text{-Bi}_4\text{O}_5\text{Br}_2$  composites modified with different contents of sulfur and/or CQDs well correspond to the standard card of  $\text{Bi}_4\text{O}_5\text{Br}_2$ , which proves that the crystal structure of  $\text{Bi}_4\text{O}_5\text{Br}_2$  remains unchanged after sulfur and CQDs are introduced. It should be noted that because the content of CQDs is low, there is no related peak is found [40]. These two tiny peaks at 38–40 degrees may can be assigned to the reduced  $\text{Bi}^0$

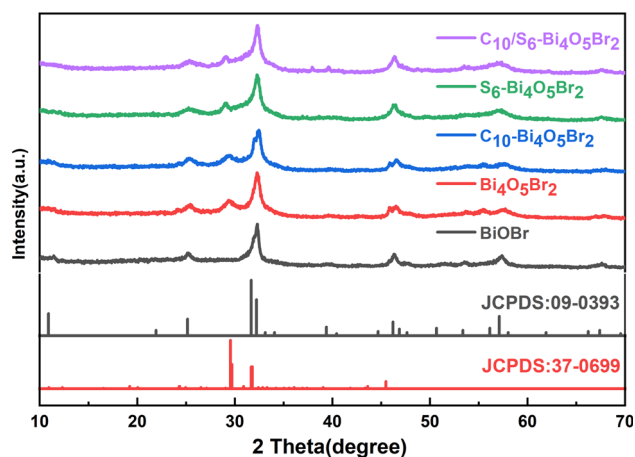


**Figure 1** XRD patterns of as-prepared samples.

(JCPDS: 44-1246), which may be due to the high content of  $\text{Bi}^{3+}$  and the reduction of a small amount of Bi by ethylene glycol.

The microstructure and morphology of the flower-like CQDs/ $S\text{-Bi}_4\text{O}_5\text{Br}_2$  composites are further studied by FESEM and HRTEM. It can be clearly seen that the prepared  $\text{BiOBr}$  sample is shown as monodisperse micron-size microspheres with a diameter of 4  $\mu\text{m}$ , in which the microspheres are formed by stacking a lot of nanosheets (Fig. 2a). Nevertheless, the prepared  $\text{Bi}_4\text{O}_5\text{Br}_2$  sample is flower-shaped microspheres with a diameter of about 1  $\mu\text{m}$  (Fig. 2b). This evolution of the morphology between these two bismuth oxybromide may be due to the fact that the self-assembled process of the  $\text{BiOBr}$  nanosheets is influenced by the transformation of perfect spheres into flower-like in the rich bismuth solution. The morphologies of the  $S\text{-Bi}_4\text{O}_5\text{Br}_2$  and CQDs/ $S\text{-Bi}_4\text{O}_5\text{Br}_2$  composites still retain the flower-like microspheres with the same size as the  $\text{Bi}_4\text{O}_5\text{Br}_2$  (Fig. 2c–e). Figure S2 shows the FESEM and HRTEM images of other  $\text{C}_{10}/\text{S}_6\text{-Bi}_4\text{O}_5\text{Br}_2$  composites with different magnification scales and TEM images of CQDs. It can be seen from the figure that the size of the prepared pristine CQDs is about 10 nm with well dispersion. Due to the low contents of S doping and CQDs modification, the structure and morphology of CQDs/ $S\text{-Bi}_4\text{O}_5\text{Br}_2$  samples are not greatly affected. Furthermore, the TEM, HRTEM, and corresponding EDS-mapping characterization are carried out to further explore the morphology with the images as shown in Fig. 2f–i. As shown from the images, the observed lattice fringes with the spacing of 0.28 nm and 0.32 nm belong to the crystal plane of  $\text{Bi}_4\text{O}_5\text{Br}_2$  (020) and the crystal plane of CQDs (002), respectively. Therefore, the HRTEM images further proves that the CQDs are successfully modified onto the S-doped  $\text{Bi}_4\text{O}_5\text{Br}_2$  to form composites. In addition, the Bi, Br, O, C, and S elements are uniformly distributed on the observed microsphere (Fig. 2j–n), which can also prove the composition of the CQDs/ $S\text{-Bi}_4\text{O}_5\text{Br}_2$  sample. Therefore, the actual content of each element in the  $\text{C}_{10}/\text{S}_6\text{-Bi}_4\text{O}_5\text{Br}_2$  composites are analyzed by the EDS characterization with the results as shown in Fig. S3. From the figure, it can be found that the content of C element in the  $\text{C}_{10}/\text{S}_6\text{-Bi}_4\text{O}_5\text{Br}_2$  composites is about 0.73% (wt. %) and the content of S is determined to be 5.09% (wt. %).

Figure 3 is the FT-IR spectra of CQDs/ $S\text{-Bi}_4\text{O}_5\text{Br}_2$  composites. It can be found that the strong characteristic



**Figure 2** FESEM image of samples: **a** BiOBr; **b** Bi<sub>4</sub>O<sub>5</sub>Br<sub>2</sub>; **c** S<sub>6</sub>-Bi<sub>4</sub>O<sub>5</sub>Br<sub>2</sub>; **d**, **e** C<sub>10</sub>/S<sub>6</sub>-Bi<sub>4</sub>O<sub>5</sub>Br<sub>2</sub>; **f**–**i** HRTEM image of C<sub>10</sub>/S<sub>6</sub>-Bi<sub>4</sub>O<sub>5</sub>Br<sub>2</sub>; **j**–**n** Elemental mapping images of each element in C<sub>10</sub>/S<sub>6</sub>-Bi<sub>4</sub>O<sub>5</sub>Br<sub>2</sub>.

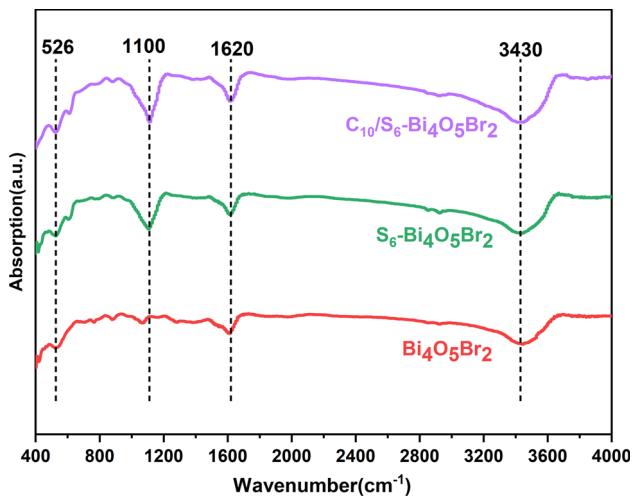
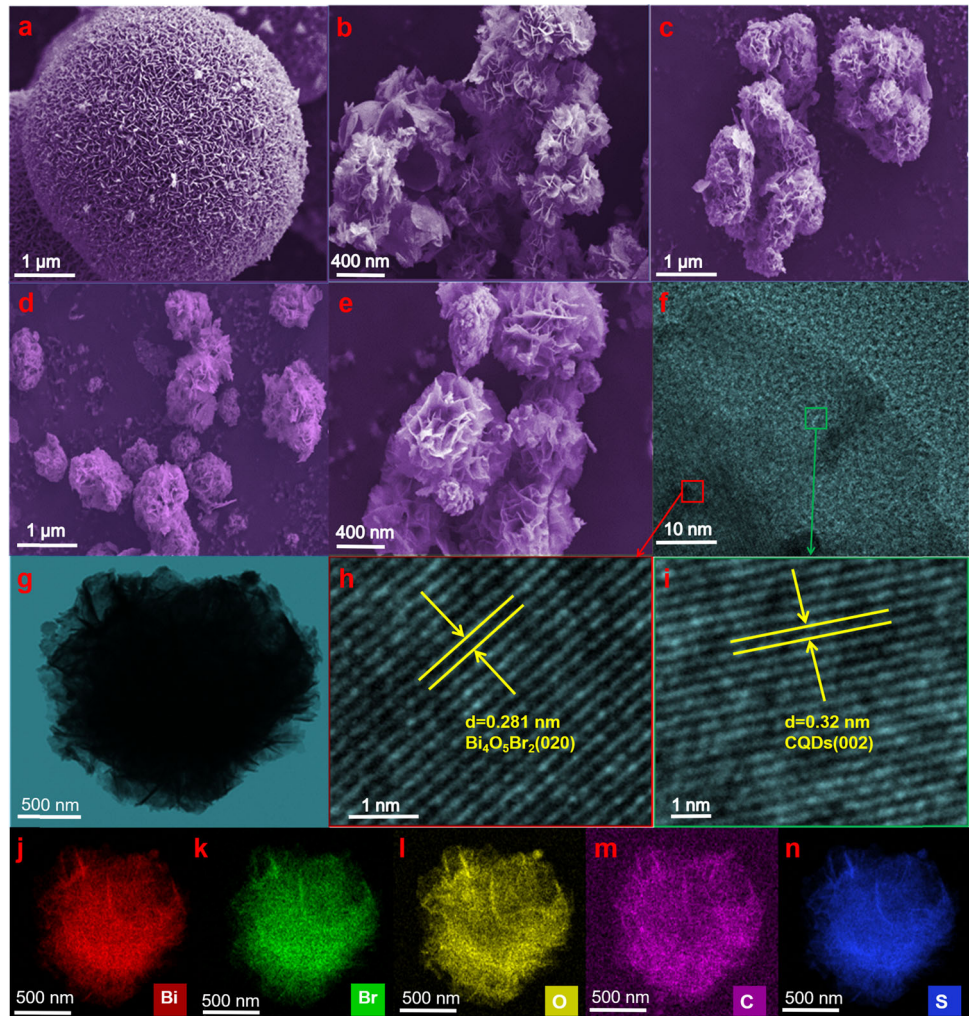


**Figure 3** FT-IR spectra for as-prepared samples.

peak at 526 cm<sup>-1</sup> of the composites is due to the Bi–O tensile vibration [41], and the two characteristic peaks

at 3430 cm<sup>-1</sup> and 1600 cm<sup>-1</sup> may correspond to O–H tensile vibration and bending vibration, respectively [32]. However, the characteristic peak at 1100 cm<sup>-1</sup> of the S<sub>6</sub>-Bi<sub>4</sub>O<sub>5</sub>Br<sub>2</sub> and C<sub>10</sub>/S<sub>6</sub>-Bi<sub>4</sub>O<sub>5</sub>Br<sub>2</sub> composites may be from the Bi–S bond, which proves that the sulfur is successfully doped into the Bi<sub>4</sub>O<sub>5</sub>Br<sub>2</sub> composite [42]. No characteristic peaks assigned to the CQDs are detected for the C<sub>10</sub>/S<sub>6</sub>-Bi<sub>4</sub>O<sub>5</sub>Br<sub>2</sub> composite, which may be due to the low content of CQDs.

Figure 4 shows the N<sub>2</sub> adsorption isotherms and the pore size distribution curves (inset) of CQDs/S-Bi<sub>4</sub>O<sub>5</sub>Br<sub>2</sub> composites. From the figure, it can be found that these four composites all show property of mesoporous materials. Compared with BiOBr, the specific surface area of other composites are relatively high. Particularly, the specific surface area of the C<sub>10</sub>/S<sub>6</sub>-Bi<sub>4</sub>O<sub>5</sub>Br<sub>2</sub> (63.942 m<sup>2</sup>/g) is 24.63 times that of BiOBr (2.596 m<sup>2</sup>/g). Therefore, the flower-like CQDs/S-Bi<sub>4</sub>O<sub>5</sub>Br<sub>2</sub> composites may show an adsorption

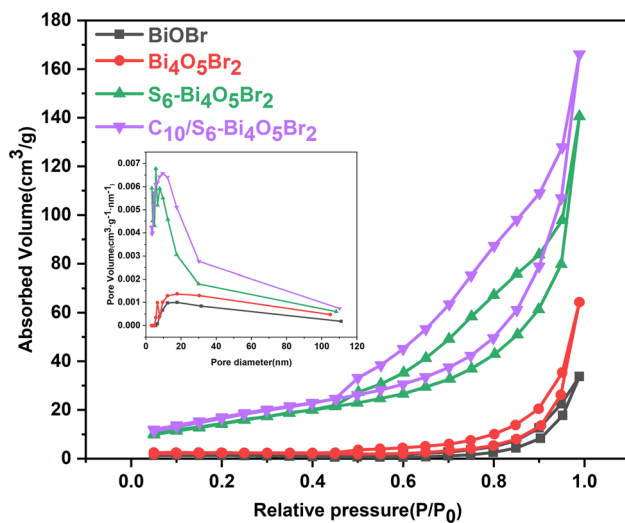


**Figure 4** N<sub>2</sub> adsorption–desorption isotherms and corresponding pore-size distribution plots (inset) of as-prepared samples.

advantage for the pollutant molecules in the photocatalytic experimental.

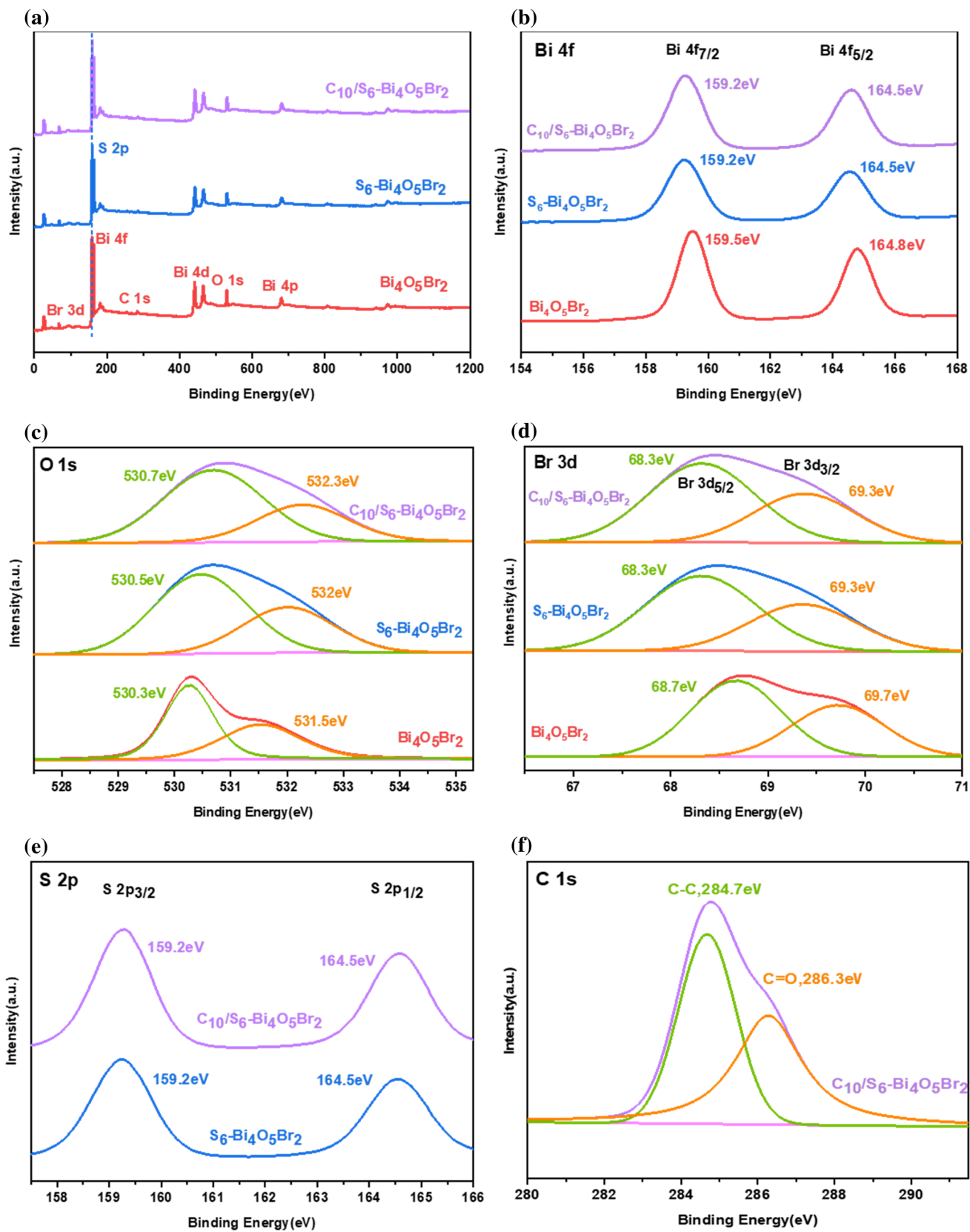
The elements in the flower-like CQDs/*S*-Bi<sub>4</sub>O<sub>5</sub>Br<sub>2</sub> composites are studied by XPS analysis with the spectra shown as in Fig. 5. Figure 5a illustrates that the peaks of *Bi*, *O*, and *Br* elements can be found in the Bi<sub>4</sub>O<sub>5</sub>Br<sub>2</sub> composite, while the extra peaks of *S* and *C* elements are observed in the C<sub>10</sub>/*S*<sub>6</sub>-Bi<sub>4</sub>O<sub>5</sub>Br<sub>2</sub> composite. It is worth noting that the appeared few characteristic peaks belonging to the C 1s in Bi<sub>4</sub>O<sub>5</sub>Br<sub>2</sub> and *S*<sub>6</sub>-Bi<sub>4</sub>O<sub>5</sub>Br<sub>2</sub> composites may be attributed to the instrument but not from the added carbonaceous material [43]. Figure 5b–f are the XPS spectra of the Bi 4*f*, O 1s, Br 3*d*, S 2*p*, and C 1s, which are used to compare the C<sub>10</sub>/*S*<sub>6</sub>-Bi<sub>4</sub>O<sub>5</sub>Br<sub>2</sub> composite with pure samples (Bi<sub>4</sub>O<sub>5</sub>Br<sub>2</sub> or *S*-Bi<sub>4</sub>O<sub>5</sub>Br<sub>2</sub>). From the Bi 4*f* spectra (Fig. 5b), the peaks at 159.5 eV and 164.8 eV are Bi 4*f*<sub>7/2</sub> and Bi 4*f*<sub>5/2</sub> of Bi<sup>3+</sup> for the Bi<sub>4</sub>O<sub>5</sub>Br<sub>2</sub> composite [44]. Furthermore, the binding energy of Bi 4*f* shifts towards the lower direction with the *S* doping. This phenomenon may be due to the fact that the radius of *S* is larger but the electronegativity smaller than the *Br* and *O* atoms, which also can explain the binding energy shift forward negative direction of the Br 3*d* and O 1s spectra compared to the undoped Bi<sub>4</sub>O<sub>5</sub>Br<sub>2</sub> composite. Exactly, as shown in the O 1s spectrum (Fig. 5c), the peak located at 530.7 eV corresponds to the Bi–O bond, and the peak at 532.3 eV may attribute to chemically adsorbed oxygen [45]. The peaks located at 68.3 eV (Br 3*d*<sub>5/2</sub>) and 69.3 eV (Br 3*d*<sub>3/2</sub>) as shown in the Br 3*d* spectrum (Fig. 5d) can be

attributed to Br<sup>−</sup> [46]. In addition, Fig. 5e shows XPS spectra of S 2*p* with the fitted binding energies located at 159.2 and 164.5 eV, which corresponds to the S 2*p*<sub>3/2</sub> and S 2*p*<sub>1/2</sub>. In addition, as shown in Fig. 5f, the binding energy peaks at 284.7 and 286.3 eV are related to C–C and C=O groups of CQDs in the C<sub>10</sub>/*S*<sub>6</sub>-Bi<sub>4</sub>O<sub>5</sub>Br<sub>2</sub> composite [47].

### Optical absorption properties

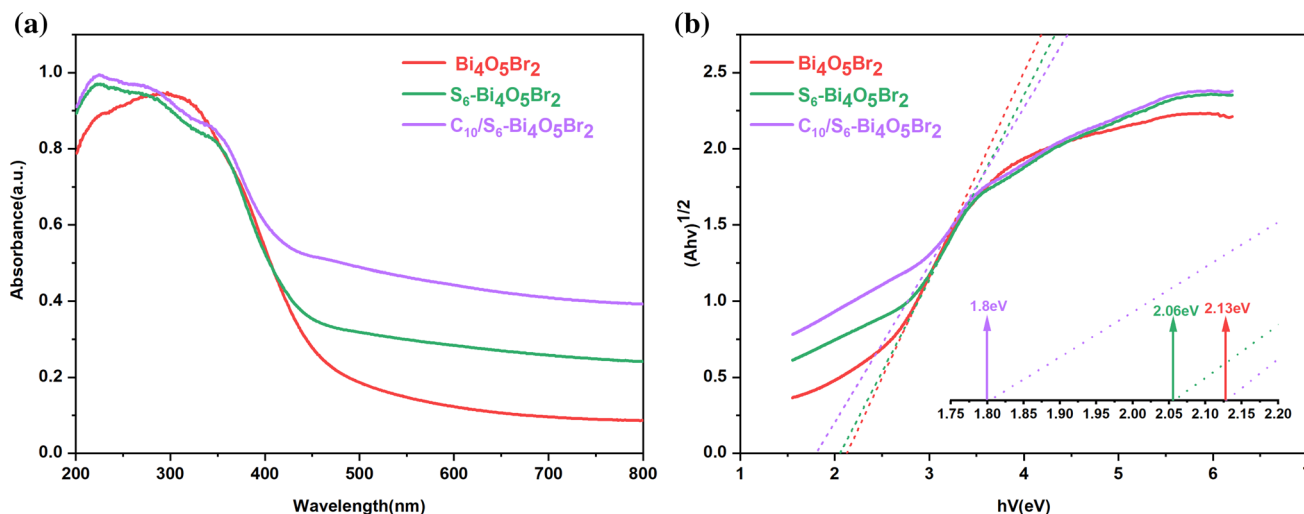
To study the influence of *S* doping and CQDs modification on the photocatalytic performance of Bi<sub>4</sub>O<sub>5</sub>Br<sub>2</sub>, the optical absorption characteristics are studied by DRS spectroscopy with the spectra as shown in Fig. 6a (200 nm < λ < 800 nm). From the figure, it is obviously found that the absorption region of the Bi<sub>4</sub>O<sub>5</sub>Br<sub>2</sub> composite is very narrow. But when the sulfur is doped, the absorption range of *S*-Bi<sub>4</sub>O<sub>5</sub>Br<sub>2</sub> composites is extended and the strength is relatively enhanced. Furthermore, when the CQDs are introduced, the light absorption range of the C<sub>10</sub>/*S*<sub>6</sub>-Bi<sub>4</sub>O<sub>5</sub>Br<sub>2</sub> shifts toward a higher wavelength with the intensity significantly enhanced. Therefore, the photon capture ability of the flower-like C<sub>10</sub>/*S*<sub>6</sub>-Bi<sub>4</sub>O<sub>5</sub>Br<sub>2</sub> composite may be effectively improved. The band gap energy (*E*<sub>g</sub>) of the prepared composites is calculated based on the UV-DRS results with the spectra as shown in Fig. 6b. As listed in the figure, the estimated *E*<sub>g</sub> of Bi<sub>4</sub>O<sub>5</sub>Br<sub>2</sub>, *S*<sub>6</sub>-Bi<sub>4</sub>O<sub>5</sub>Br<sub>2</sub>, and C<sub>10</sub>/*S*<sub>6</sub>-Bi<sub>4</sub>O<sub>5</sub>Br<sub>2</sub> is 2.13 eV, 2.06 eV, and 1.8 eV, respectively. Therefore, it can be concluded that the *S* doping and introduction of CQDs could reduce the *E*<sub>g</sub> of the composite, and then improve the absorption capacity of visible light.

Figure 7 is the Mott–Schottky (MS) measurement diagram of CQDs/*S*-Bi<sub>4</sub>O<sub>5</sub>Br<sub>2</sub> composites. As shown in the figure, the slopes of the curves for these three composites are positive, which proves that the prepared Bi<sub>4</sub>O<sub>5</sub>Br<sub>2</sub>, *S*<sub>6</sub>-Bi<sub>4</sub>O<sub>5</sub>Br<sub>2</sub>, and C<sub>10</sub>/*S*<sub>6</sub>-Bi<sub>4</sub>O<sub>5</sub>Br<sub>2</sub> photocatalysts are *n*-type semiconductors. Furthermore, the flat-band potential of Bi<sub>4</sub>O<sub>5</sub>Br<sub>2</sub>, *S*<sub>6</sub>-Bi<sub>4</sub>O<sub>5</sub>Br<sub>2</sub>, and C<sub>10</sub>/*S*<sub>6</sub>-Bi<sub>4</sub>O<sub>5</sub>Br<sub>2</sub> composites are estimated to be −0.31, −0.35, and −0.39 V *vs.* SCE (calomel electrode), respectively. Generally speaking, the conduction band (CB) potential of *n*-type semiconductors is 0.2 V smaller than the flat band potential [48]. Thus, the CB potentials of the Bi<sub>4</sub>O<sub>5</sub>Br<sub>2</sub>, *S*<sub>6</sub>-Bi<sub>4</sub>O<sub>5</sub>Br<sub>2</sub> and C<sub>10</sub>/*S*<sub>6</sub>-Bi<sub>4</sub>O<sub>5</sub>Br<sub>2</sub> composites are calculated to be −0.51, −0.55 and −0.59 V *vs.* SCE at pH = 7 (equivalent to −0.27, −0.31, and −0.35 V *vs.* NHE



**Figure 5** XPS survey spectrum of a photocatalysts and corresponding XPS spectra: **b** Bi 4*f*; **c** O 1*s*; **d** Br 3*d*; **e** S 2*p*; **f** C 1*s*.





**Figure 6** a UV–DRS spectra; b Tauc plots of as-prepared samples.

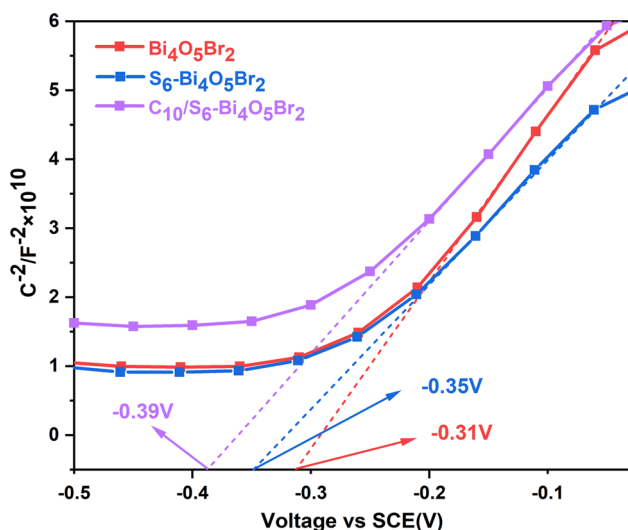


**Figure 7** The MS plots for estimating flat-band potentials of the as-prepared CQDs/ $S\text{-Bi}_4\text{O}_5\text{Br}_2$  composites.

(normal hydrogen electrode)), respectively. Therefore, according to the obtained  $E_g$  value, the valence band (VB) potentials of the samples are thus calculated to be 1.86, 1.75, and 1.65 V vs. NHE at pH = 7, respectively.

### Photocatalytic activity analysis

The photocatalytic performance of CQDs/ $S\text{-Bi}_4\text{O}_5\text{Br}_2$  composites was evaluated by photodegradation of CIP under simulated visible light irradiation. Figure 8a shows the CIP photodegradation curve for the S-doped  $\text{Bi}_4\text{O}_5\text{Br}_2$  photocatalyst. From the figure, it can be clearly seen that there is almost no change of

the CIP concentration without any photocatalyst added, which indicates the good stability of CIP under irradiation. Before the light source is turned on, the CQDs/ $S\text{-Bi}_4\text{O}_5\text{Br}_2$  photocatalysts are dispersed into the CIP solution for 30 min without a light source to eliminate the influence of adsorption on degradation. From the figures, it is easily found that the concentration of CIP solution is not changed after 10 min stirring, which indicates that 30 min for the adsorption–desorption equilibrium establishment is enough. Compared with the un-doped ozone bismuth composites ( $\text{BiOBr}$  and  $\text{Bi}_4\text{O}_5\text{Br}_2$ ), the S-doping  $\text{Bi}_4\text{O}_5\text{Br}_2$  shows a much higher photodegradation rate of CIP, especially for the  $S_6\text{-Bi}_4\text{O}_5\text{Br}_2$  composite. The degradation rate of  $S_6\text{-Bi}_4\text{O}_5\text{Br}_2$  is as high as 80.2% within 60 min. Furthermore, with the CQDs introduction, the CQDs/ $S\text{-Bi}_4\text{O}_5\text{Br}_2$  composites show much better photocatalytic performance compared to the pure ones ( $\text{Bi}_4\text{O}_5\text{Br}_2$  and  $S_6\text{-Bi}_4\text{O}_5\text{Br}_2$ ) (Fig. 8b). The most striking is that the  $C_{10}/S_6\text{-Bi}_4\text{O}_5\text{Br}_2$  composite with an appropriate content of CQDs shows excellent performance with the degradation rate of 93.5% within 60 min. This may be due to the fact that the visible light absorption capacity of the CQDs/ $S_6\text{-Bi}_4\text{O}_5\text{Br}_2$  composites could effectively be enhanced when the CQDs are introduced [49]. It is worth noting that when the introduced CQDs are too much, the active site of the  $S_6\text{-Bi}_4\text{O}_5\text{Br}_2$  composite might be blocked, and then the photocatalytic performance will be weakened. Figure 8c shows the kinetic equation diagram of CIP degradation for the prepared composites. It can be found that  $C_{10}/S_6\text{-Bi}_4\text{O}_5\text{Br}_2$



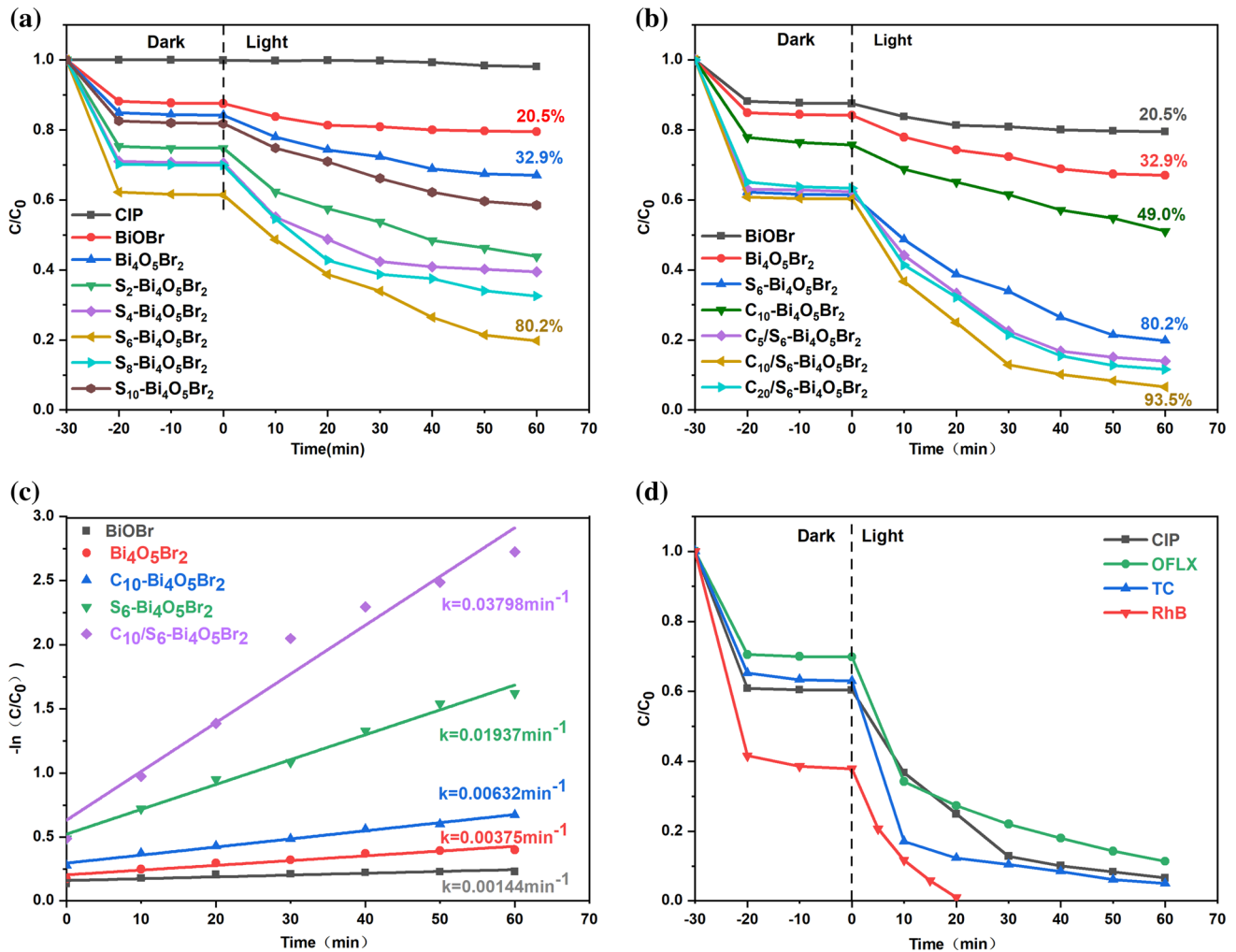


**Figure 8** Photocatalytic activity of the samples **a, b** for the CIP degradation, **c** for the Kinetics of CIP degradation, **d** for the degradation of different pollutants.

shows the highest  $k$  value ( $0.03798 \text{ min}^{-1}$ ) for CIP photodegradation, which is 1.96, 6.01, 10.13 and 26.38 times than that of S<sub>6</sub>-Bi<sub>4</sub>O<sub>5</sub>Br<sub>2</sub> ( $0.01937 \text{ min}^{-1}$ ), C<sub>10</sub>-Bi<sub>4</sub>O<sub>5</sub>Br<sub>2</sub> ( $0.00632 \text{ min}^{-1}$ ), Bi<sub>4</sub>O<sub>5</sub>Br<sub>2</sub> ( $0.00375 \text{ min}^{-1}$ ) and BiOBr ( $0.00144 \text{ min}^{-1}$ ), respectively. To further investigate photocatalytic performance of the flower-like C<sub>10</sub>/S<sub>6</sub>-Bi<sub>4</sub>O<sub>5</sub>Br<sub>2</sub> composite, other three different types of substance are selected as a simulated pollutant to be photodegraded under the same condition (Fig. 8d). It can be found from the figure that the photodegradation efficiencies of the C<sub>10</sub>/S<sub>6</sub>-Bi<sub>4</sub>O<sub>5</sub>Br<sub>2</sub> composite are very high, and the efficiencies of C<sub>10</sub>/S<sub>6</sub>-Bi<sub>4</sub>O<sub>5</sub>Br<sub>2</sub> composite are close to 100% for RhB, 93.5% for CIP, 95% for TC and 88% for OFLX under visible-light irradiation within 20, 60, 60, 60 min, respectively. Therefore, C<sub>10</sub>/S<sub>6</sub>-Bi<sub>4</sub>O<sub>5</sub>Br<sub>2</sub> composite may hold a competitive photocatalytic activity for

different kind of pollutants under visible light irradiation. Additionally, the photocatalytic performances of the prepared flower-like C<sub>10</sub>/S<sub>6</sub>-Bi<sub>4</sub>O<sub>5</sub>Br<sub>2</sub> composite for the CIP and RhB degradation under visible light are further compared with related photocatalysts reported on some studies published in recent years (exactly as shown in Table S1) [36, 50–56]. It is easy to find that the C<sub>10</sub>/S<sub>6</sub>-Bi<sub>4</sub>O<sub>5</sub>Br<sub>2</sub> composite in this work exhibits a predominant catalytic activity compared to the other listed photocatalysts. Remarkably, compared to the similar C<sub>3</sub>N<sub>4</sub>-Bi<sub>4</sub>O<sub>5</sub>Br<sub>2</sub> and BiOBr/CDS/C<sub>3</sub>N<sub>4</sub> composites, the C<sub>10</sub>/S<sub>6</sub>-Bi<sub>4</sub>O<sub>5</sub>Br<sub>2</sub> photocatalyst displays a much higher CIP degradation rate under the visible light irradiation, which is a strong evidence for the microstructural privilege of the 3D flower-like structure with reasonable band gap structure caused by the S-

doping and CQDs introduction. The comparison results prove that the prepared flower-like  $C_{10}/S_6-Bi_4O_5Br_2$  composite may show great application potential in the organic wastewater treatment field.

Photocatalyst not only needs excellent photocatalytic performance but also needs enough stability, which plays a vital role in its practical application [57]. Therefore, CIP degradation experiments are carried out for four cycles with the flower-like  $C_{10}/S_6-Bi_4O_5Br_2$  composite as the photocatalyst (Fig. S4a). The figure shows that the CIP degradation rate for the  $C_{10}/S_6-Bi_4O_5Br_2$  just shows a slight decrease (from 95.5% to 83.3%) after four cycles tests, indicating that the composite possesses excellent photocatalytic stability under simulated visible light irradiation. Furthermore, the  $C_{10}/S_6-Bi_4O_5Br_2$  composite is characterized by XRD after cycle tests with the patterns shown as in Fig. S4b. From the figure, it is obviously found that the XRD pattern of  $C_{10}/S_6-Bi_4O_5Br_2$  before and after cyclic testing show no significant changes, indicating that the crystal structure of the flower-like  $C_{10}/S_6-Bi_4O_5Br_2$  composite is maintained during the photocatalytic reaction process. Therefore, it is expected that the prepared flower-like  $C_{10}/S_6-Bi_4O_5Br_2$  composite may be an ideal photocatalyst in the wastewater treatment field.

### DFT calculation

To further understand the relationship between the microstructure and properties of the  $Bi_4O_5Br_2$  composites, the electronic structure was calculated by the CASTEP module based on DFT. The optimized structures of the CQDs and  $Bi_4O_5Br_2$  are shown in Fig. S5a–b, at the same time, Fig. S5c–d is the two types of S-doping sites (O sites and Br sites). As shown in Fig. S5e that the formation energy of S atoms in O sites is lower than that of Br sites, which indicates that the S atoms are more easily doped into O sites in  $Bi_4O_5Br_2$  structure.

To understand the charge transfer path, the electrostatic potentials of  $Bi_4O_5Br_2$ ,  $S-Bi_4O_5Br_2$ , and CQDs surface models are calculated. As shown in Fig. 9a–c, the work functions ( $\Phi$ ) of  $Bi_4O_5Br_2$ ,  $S-Bi_4O_5Br_2$ , and CQDs surface are calculated to be 6.86, 6.82, and 3.24 eV, respectively. It is obviously found that the  $\Phi$  value of  $S-Bi_4O_5Br_2$  is little lower than that of undoped  $Bi_4O_5Br_2$ , which means that S doping is beneficial for electrons to escape from the surface of  $Bi_4O_5Br_2$  and then accelerate the photo-induced

charge migration. When the CQDs are introduced into the  $S-Bi_4O_5Br_2$  composites, the work function of  $S-Bi_4O_5Br_2$  is much greater than CQDs, therefore the electrons will transfer from  $S-Bi_4O_5Br_2$  to CQDs to find an equilibrated fermi level. Afterward, an internal electric field is formed from CQDs to  $S-Bi_4O_5Br_2$ . And then the formed internal electric field could further facilitate the separation and transfer efficiency of the photogenerated carriers from  $S-Bi_4O_5Br_2$  to CQDs. Moreover, this charge transfer pathway is also kinetically favorable according to the results of calculated charge effective masses.

The electronic density of states of  $Bi_4O_5Br_2$  and  $S-Bi_4O_5Br_2$  models are calculated. Figure 10a shows that the valence band energy level of  $Bi_4O_5Br_2$  is mainly composed of Br 4p and O 2p, while the conduction band is mainly composed of the hybridization of Bi 6p orbital electrons. For the  $S-Bi_4O_5Br_2$  model (Fig. 10b), it is obviously found that the doping level of S 2p near the fermi level is introduced with the doping of S element. The introduction of doping energy level can hybridize with O 2p orbital electrons to form a new conduction band. It can be concluded that the conduction band of  $Bi_4O_5Br_2$  shifts upwards which is caused by the S doping. And the band gap of the  $S-Bi_4O_5Br_2$  composites is then decreased which is helpful to improve photocatalytic activity.

### Photo-induced charge properties

Figure 11 is the photoluminescence spectrum of the prepared CQDs/ $S-Bi_4O_5Br_2$  composites. From the figure, it can be found that all the composites show a peak around 465 nm after excitation from the light with the wavelength at 325 nm. Otherwise, the fluorescence intensity of the  $C_{10}/S_6-Bi_4O_5Br_2$  sample is lower than that of  $S_6-Bi_4O_5Br_2$ , and the latter one is much lower than the  $Bi_4O_5Br_2$ . Therefore, it is believed that the recombination rate of photoelectron-hole pair in the flower-like  $C_{10}/S_6-Bi_4O_5Br_2$  is the lowest, then it also means that the separation of surface charges in the composite is more effective than the others and thus the photocatalytic performance is promoted.

To further explain the possible mechanism of CIP degradation, free radical trapping experiments are carried out in this work [58]. Generally, three active ions ( $\cdot OH$ ,  $h^+$  and  $\cdot O_2^-$ ) are the most common and important substances participating. Therefore, the

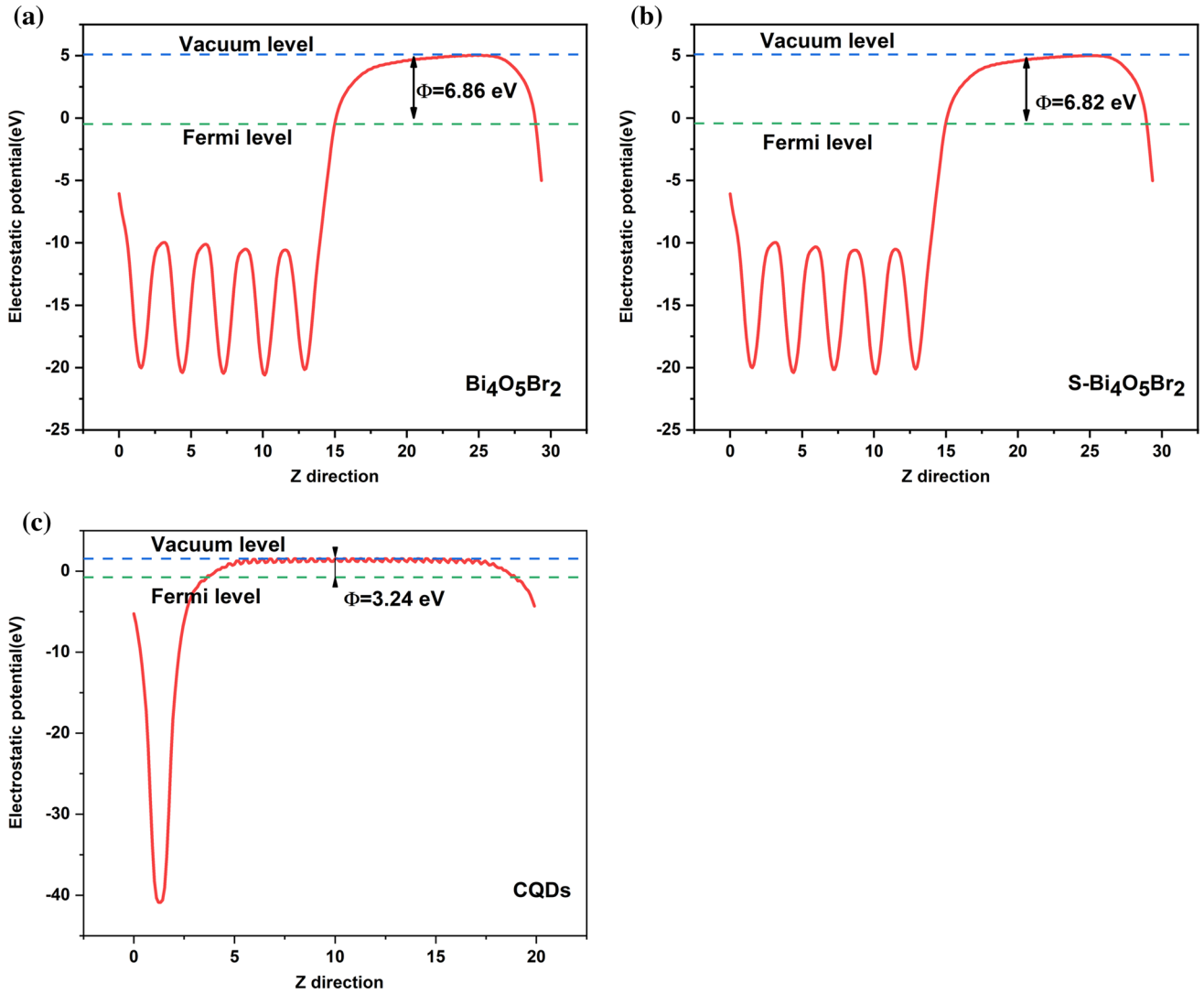


Figure 9 Calculated electrostatic potentials of a  $\text{Bi}_4\text{O}_5\text{Br}_2$ ; b  $\text{S-Bi}_4\text{O}_5\text{Br}_2$ ; c CQDs.

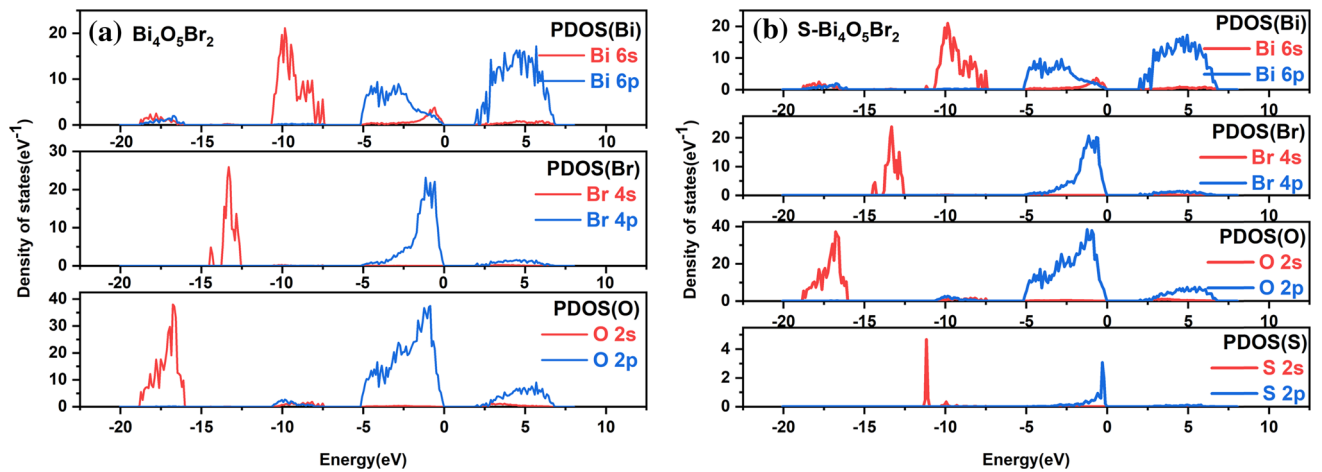
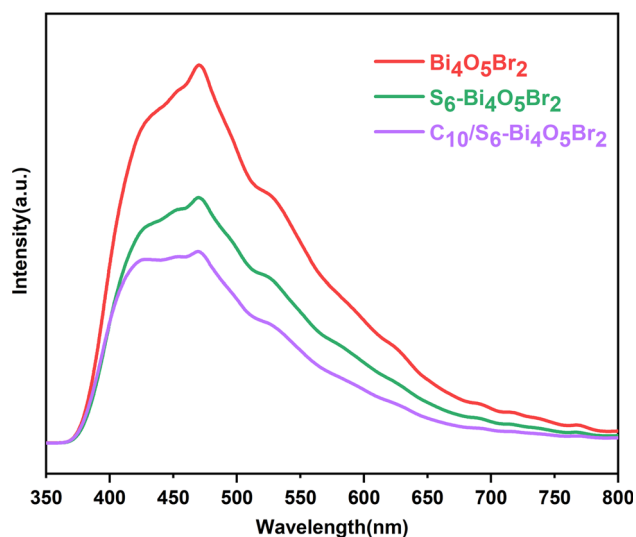


Figure 10 Calculated DOS: a  $\text{Bi}_4\text{O}_5\text{Br}_2$  and b  $\text{S-Bi}_4\text{O}_5\text{Br}_2$ .



**Figure 11** PL spectra of the as-prepared samples.

IPA, EDTA-2Na, and BQ are chosen as active ions scavengers in this experiment. It is obviously found that the IPA shows the least effect on CIP degradation, but the EDTA-2Na and BQ greatly reduce the CIP degradation rate (Fig. 12a–b). Exactly, the CIP degradation rate is decreased from 93.5% to 46.3% in 60 min with the EDTA-2Na addition, and for the BQ is from 93.5% to 53.7% on the same reaction time. Therefore, the experimental results show that the  $h^+$  and  $\cdot O_2^-$  play an indispensable role during the CIP degradation on  $C_{10}/S_6-Bi_4O_5Br_2$  photocatalyst. For further detecting the generation of free radicals, ESR measurements of the  $C_{10}/S_6-Bi_4O_5Br_2$  composite are carried out which is listed in Fig. 12c–d [59]. From Fig. 12c, it is obviously found that no ESR signal of  $\cdot O_2^-$  is observed for the test sample in dark condition. With the increase of illumination time, there are four typical signal peaks appeared and the signal peaks become larger and larger, which corresponds to the characteristic peaks of the  $\cdot O_2^-$ . On the other hand, as shown in Fig. 12d, the longer the illumination time, the weaker the three signal peaks corresponding to  $h^+$ . Therefore, the radical trapping experiments and ESR study both prove that the produced  $\cdot O_2^-$  and  $h^+$  play crucial roles for the CIP degradation process with the  $C_{10}/S_6-Bi_4O_5Br_2$  as effective photocatalyst.

The charge transfer performance of the prepared CQDs/ $S-Bi_4O_5Br_2$  composites are further characterized by the EIS test. As shown by the Nyquist

diagram of impedance spectra in Fig. 13a, the  $C_{10}/S_6-Bi_4O_5Br_2$  composite shows the smallest radius compared to the other prepared composites, indicating that it may show the highest charge separation efficiency. Figure 13b is a transient photocurrent response diagram of the prepared composites. It can be observed that the photocurrent density of the flower-like  $C_{10}/S_6-Bi_4O_5Br_2$  composite is the highest among these tested samples, which is stable at about  $6 \mu A cm^{-2}$  under the visible light irradiation. Therefore, it proves that the photo-generated charge carrier separation in the flower-like  $C_{10}/S_6-Bi_4O_5Br_2$  composite is most effective [60].

According to the characterization and discussions, the possible mechanism of organic pollutants degradation and internal charge transfer path diagram on the prepared flower-like  $C_{10}/S_6-Bi_4O_5Br_2$  composite are proposed with the figure shown as in Fig. 14. Because of the S-doping, the appeared doping level may be introduced into the band gap of  $C_{10}/S_6-Bi_4O_5Br_2$  composite, which causes the obvious enhancement of photocatalytic effect. The CQDs with excellent electronic conductivity are introduced into the S-doped  $Bi_4O_5Br_2$  composites as the charge mediator. Because of the bridging effect between these two substances, the separation efficiency of optical carriers is further improved. Furthermore, the CQDs could also absorb the light with a large wavelength and emit another one with a small wavelength [35], then more electrons will be stimulated and then generate the  $\cdot O_2^-$  active species. Peculiarly, the separation of photogenerated electrons may lead to the collection of  $h^+$  on the doping level with the S doping, then the organic pollutants are oxidized to decompose. According to the analysis, the activity of  $C_{10}/S_6-Bi_4O_5Br_2$  is significantly improved due to its special flower-like structure, reasonable band gap structure caused by the S-doping, and the CQDs introduction.

## Conclusion

In this paper, the bismuth-rich flower-like  $C_{10}/S_6-Bi_4O_5Br_2$  composite is prepared through a one-step in-situ reaction process with the sulfur and the CQDs introduced as the charge mediator. Comparatively,



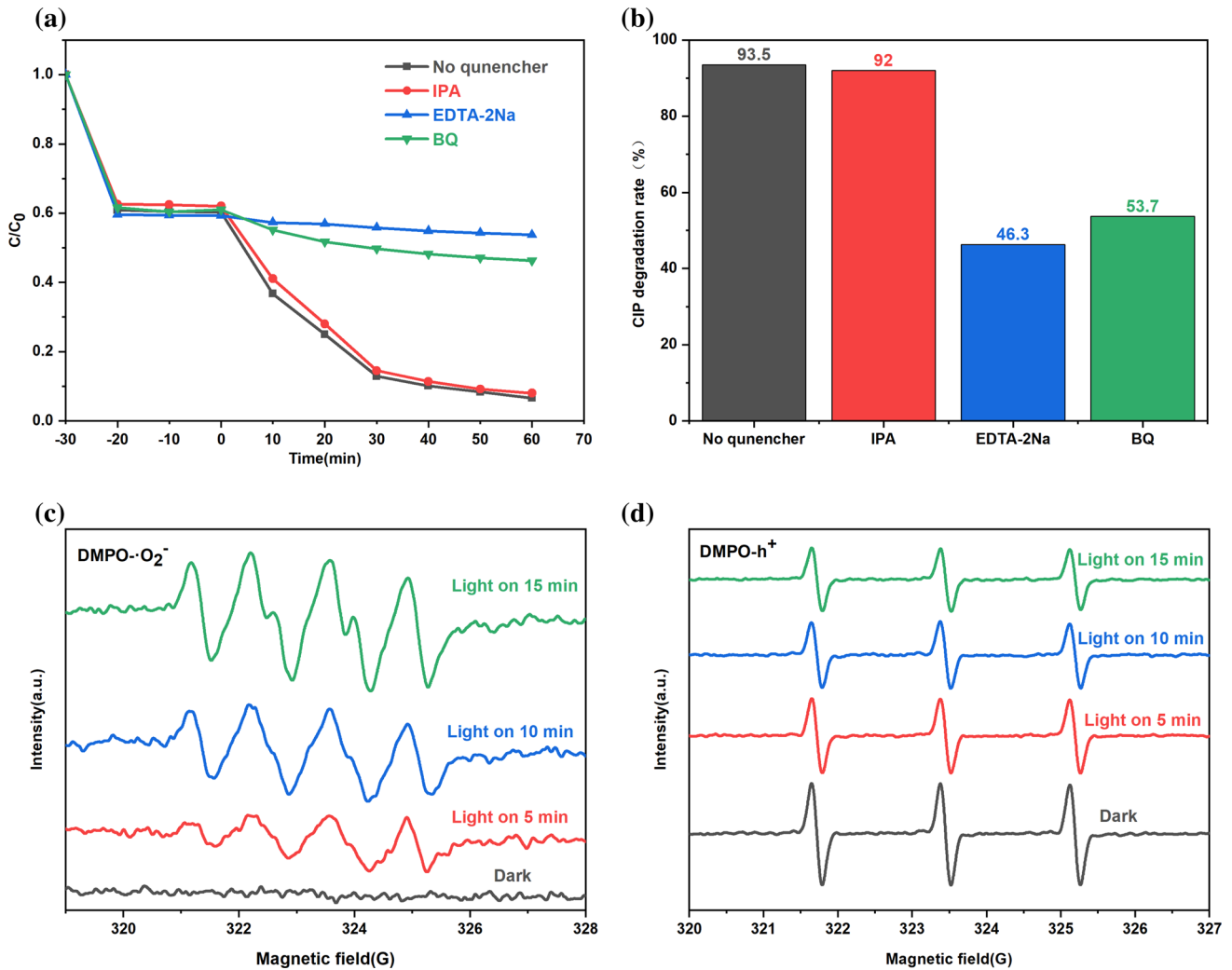


**Figure 12** a, b Free radical trapping experiments c ESR spectra of  $DMPO \cdot O_2^-$  adduct and d  $DMPO \cdot h^+$  adduct over the prepared  $C_{10}/S_6-Bi_4O_5Br_2$  composite.

the  $C_{10}/S_6-Bi_4O_5Br_2$  composite shows a good photocatalytic activity and stability for CIP photodegradation with the apparent rate constants  $k$  of  $0.03798 \text{ min}^{-1}$ , which is 26.3 times and 10.1 times higher than that of the pure  $BiOBr$  and  $Bi_4O_5Br_2$ , respectively. At the same time, it also shows a high degradation effect for other pollutants. The excellent activity of  $C_{10}/S_6-Bi_4O_5Br_2$  can be attributed to the special flower-like structure, reasonable band gap structure caused by the S-doping, and the existence

of CQDs with the improved adsorption of the light. According to the capture experiment results and ESR test, it is proved that the produced  $\cdot O_2^-$  and  $h^+$  radical play crucial roles for the CIP degradation. Therefore, the prepared flower-like  $C_{10}/S_6-Bi_4O_5Br_2$  composite can effectively degrade the different kinds of pollutants under the absolutely visible light conditions. Furthermore, this study can be used as a new reference for the bismuth oxyhalide photocatalyst in environmental restoration.

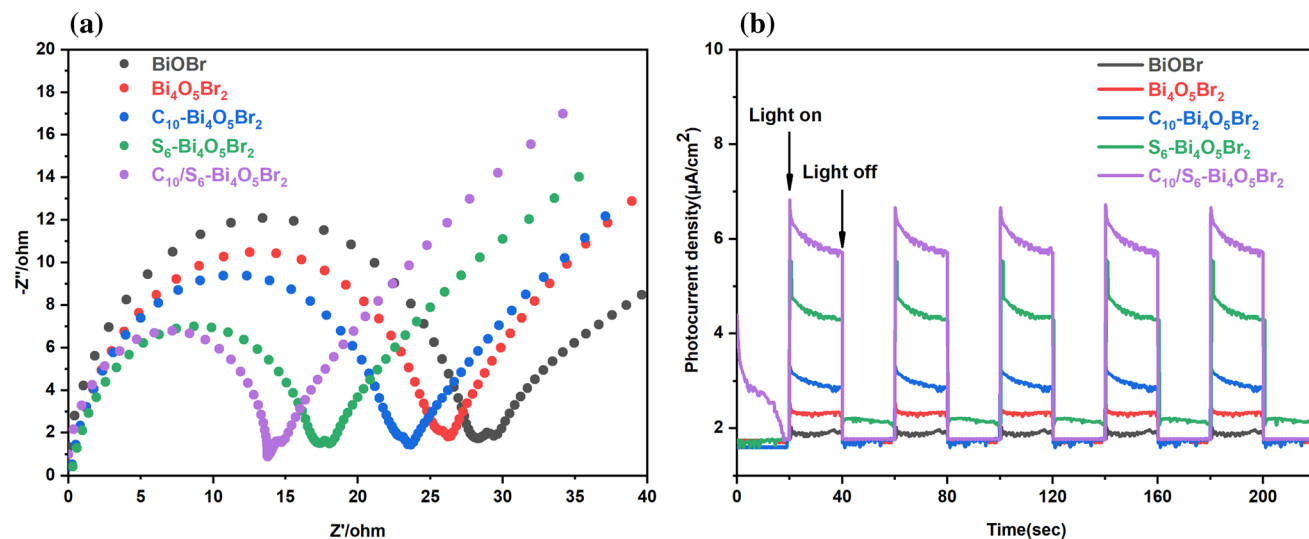


**Figure 13** a EIS and b transient photocurrent responses diagram of the prepared samples.

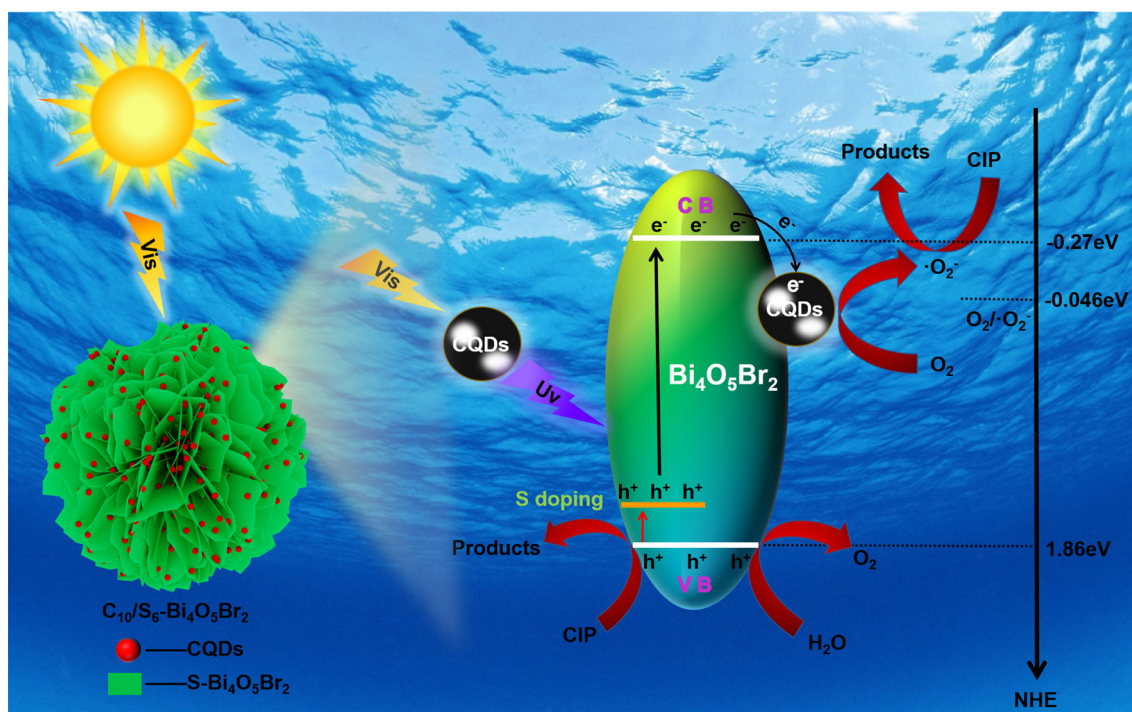


**Figure 14** Scheme of the photocatalytic mechanism of  $C_{10}/S_6-Bi_4O_5Br_2$  under visible-light irradiation.

## Acknowledgements

This project was financially supported by the Scientific Research Plan Project of the Education Department of the Hubei Province [grant number B2019377], the Open Project of Key Laboratory of Green Chemical Process of Ministry of Education [grant number GCP20190205].

## Declarations

**Conflict of interest** The authors declare that there is no conflict of interest regarding the publication of this paper.

**Supplementary Information:** The online version contains supplementary material available at <http://doi.org/10.1007/s10853-021-06661-z>.

## References:

- [1] Rashid J, Abbas A, Chang LC et al (2019) Butterfly cluster like lamellar BiOBr/TiO<sub>2</sub> nanocomposite for enhanced sunlight photocatalytic mineralization of aqueous ciprofloxacin. *Sci Total Environ* 665:668–677. <https://doi.org/10.1016/j.scitotenv.2019.02.145>
- [2] Ren X, Zhang X, Guo R et al (2021) Hollow mesoporous g-C<sub>3</sub>N<sub>4</sub>/Ag<sub>2</sub>CrO<sub>4</sub> photocatalysis with direct Z-scheme: excellent degradation performance for antibiotics and dyes. *Sep Purif Technol* 270:118797. <https://doi.org/10.1016/j.seppur.2021.118797>
- [3] Cheng H, Huang B, Dai Y (2014) Engineering BiOX (X = Cl, Br, I) nanostructures for highly efficient photocatalytic applications. *Nanoscale* 6:2009–2026. <https://doi.org/10.1039/c3nr05529a>
- [4] Ge M, Li Q, Cao C et al (2017) One-dimensional TiO<sub>2</sub> nanotube photocatalysts for solar water splitting. *Adv Sci* 4:1600152. <https://doi.org/10.1002/advs.201600152>
- [5] Liu J, Wang G, Li B, Ma X, Hu Y, Cheng H (2021) A high-efficiency mediator-free Z-scheme Bi<sub>2</sub>MoO<sub>6</sub>/AgI heterojunction with enhanced photocatalytic performance. *Sci Total Environ* 784:147227–147227. <https://doi.org/10.1016/j.scitotenv.2021.147227>
- [6] Han X, Kuang Q, Jin M, Xie Z, Zheng L (2009) Synthesis of titania nanosheets with a high percentage of exposed (001) facets and related photocatalytic properties. *J Am Chem Soc* 131:3152–3153. <https://doi.org/10.1021/ja8092373>
- [7] Neatu S, Antonio Macia-Agullo J, Concepcion P, Garcia H (2014) Gold-copper nanoalloys supported on TiO<sub>2</sub> as photocatalysts for CO<sub>2</sub> reduction by water. *J Am Chem Soc* 136:15969–15976. <https://doi.org/10.1021/ja506433k>
- [8] Dai Y, Li C, Shen Y et al (2018) Efficient solar-driven hydrogen transfer by bismuth-based photocatalyst with engineered basic sites. *J Am Chem Soc* 140:16711–16719. <https://doi.org/10.1021/jacs.8b09796>
- [9] Di J, Xia J, Ji M et al (2016) Advanced photocatalytic performance of graphene-like BN modified BiOBr flower-like materials for the removal of pollutants and mechanism insight. *Appl Catal B Environ* 183:254–262. <https://doi.org/10.1016/j.apcatb.2015.10.036>
- [10] Ye L, Jin X, Leng Y, Su Y, Xie H, Liu C (2015) Synthesis of black ultrathin BiOCl nanosheets for efficient photocatalytic H<sub>2</sub> production under visible light irradiation. *J Power Sour* 293:409–415. <https://doi.org/10.1016/j.jpowsour.2015.05.101>
- [11] Liu J, Li R, Zu X et al (2019) Photocatalytic conversion of nitrogen to ammonia with water on triphase interfaces of hydrophilic-hydrophobic composite Bi<sub>4</sub>O<sub>5</sub>Br<sub>2</sub>/ZIF-8. *Chem Eng J* 371:796–803. <https://doi.org/10.1016/j.cej.2019.03.283>
- [12] Kong XY, Lee WQ, Mohamed AR, Chai S-P (2019) Effective steering of charge flow through synergistic inducing oxygen vacancy defects and p-n heterojunctions in 2D/2D surface-engineered Bi<sub>2</sub>WO<sub>6</sub>/BiOI cascade: towards superior photocatalytic CO<sub>2</sub> reduction activity. *Chem Eng J* 372:1183–1193. <https://doi.org/10.1016/j.cej.2019.05.001>
- [13] Wang Q, Wang W, Zhong L, Liu D, Cao X, Cui F (2018) Oxygen vacancy-rich 2D/2D BiOCl-g-C<sub>3</sub>N<sub>4</sub> ultrathin heterostructure nanosheets for enhanced visible-light-driven photocatalytic activity in environmental remediation. *Appl Catal B Environ* 220:290–302. <https://doi.org/10.1016/j.apcatb.2017.08.049>
- [14] Wang C-Y, Zeng Q, Zhu G (2021) Novel S-doped BiOBr nanosheets for the enhanced photocatalytic degradation of bisphenol A under visible light irradiation. *Chemosphere* 268:128854–128854. <https://doi.org/10.1016/j.chemosphere.2020.128854>
- [15] Jin X, Lv C, Zhou X et al (2019) A bismuth rich hollow Bi<sub>4</sub>O<sub>5</sub>Br<sub>2</sub> photocatalyst enables dramatic CO<sub>2</sub> reduction activity. *Nano Energy* 64:103955. <https://doi.org/10.1016/j.nanoen.2019.103955>
- [16] Liu N, Xie H, Li J, Zhao Y, Wang N (2020) Synthesis and high visible light photocatalytic activity of ternary brookite-g-C<sub>3</sub>N<sub>4</sub>-BiOBr composite. *NANO* 15:2050042. <https://doi.org/10.1142/s1793292020500459>
- [17] Di J, Xia J, Li H, Guo S, Dai S (2017) Bismuth oxyhalide layered materials for energy and environmental applications. *Nano Energy* 41:172–192. <https://doi.org/10.1016/j.nanoen.2017.09.008>
- [18] Wang S, Hai X, Ding X et al (2017) Light-switchable oxygen vacancies in ultrafine Bi<sub>5</sub>O<sub>7</sub>Br nanotubes for boosting solar-driven nitrogen fixation in pure water. *Adv Mater* 29:1701774. <https://doi.org/10.1002/adma.201701774>
- [19] Wang J, Yu Y, Zhang L (2013) Highly efficient photocatalytic removal of sodium pentachlorophenate with Bi<sub>3</sub>O<sub>4</sub>Br under visible light. *Appl Catal B Environ* 136:112–121. <https://doi.org/10.1016/j.apcatb.2013.02.009>
- [20] Di J, Xia J, Ji M et al (2015) Controllable synthesis of Bi<sub>4</sub>O<sub>5</sub>Br<sub>2</sub> ultrathin nanosheets for photocatalytic removal of ciprofloxacin and mechanism insight. *J Mater Chem A* 3:15108–15118. <https://doi.org/10.1039/c5ta02388b>
- [21] Li R, Xie F, Liu J, Zhang C, Zhang X, Fan C (2019) Room-temperature hydrolysis fabrication of BiOBr/Bi<sub>12</sub>O<sub>17</sub>Br<sub>2</sub> Z-Scheme photocatalyst with enhanced resorcinol degradation and NO removal activity. *Chemosphere* 235:767–775. <https://doi.org/10.1016/j.chemosphere.2019.06.231>
- [22] Zhou L, Zhuang Z, Zhao H, Lin M, Zhao D, Mai L (2017) Intricate hollow structures: controlled synthesis and

- applications in energy storage and conversion. *Adv Mater* 29:1602914. <https://doi.org/10.1002/adma.201602914>
- [23] Lu F, Cai W, Zhang Y (2008) ZnO hierarchical micro/nanoarchitectures: solvothermal synthesis and structurally enhanced photocatalytic performance. *Adv Func Mater* 18:1047–1056. <https://doi.org/10.1002/adfm.200700973>
- [24] Zhu L-P, Liao G-H, Bing N-C, Wang L-L, Yang Y, Xie H-Y (2010) Self-assembled 3D BiOCl hierarchitectures: tunable synthesis and characterization. *CrystEngComm* 12:3791–3796. <https://doi.org/10.1039/c0ce00038h>
- [25] Yang L, Liang L, Wang L, Zhu J, Gao S, Xia X (2019) Accelerated photocatalytic oxidation of carbamazepine by a novel 3D hierarchical protonated g-C<sub>3</sub>N<sub>4</sub>/BiOBr heterojunction: performance and mechanism. *Appl Surf Sci* 473:527–539. <https://doi.org/10.1016/j.apsusc.2018.12.180>
- [26] Rosales M, Zoltan T, Yadarola C, Mosquera E, Gracia F, Garcia A (2019) The influence of the morphology of 1D TiO<sub>2</sub> nanostructures on photogeneration of reactive oxygen species and enhanced photocatalytic activity. *J Mol Liq* 281:59–69. <https://doi.org/10.1016/j.molliq.2019.02.070>
- [27] Zhuang H, Zhang Y, Chu Z et al (2016) Synergy of metal and nonmetal dopants for visible-light photocatalysis: a case-study of Sn and N co-doped TiO<sub>2</sub>. *Phys Chem Chem Phys* 18:9636–9644. <https://doi.org/10.1039/c6cp00580b>
- [28] Abdelraheem WHM, Patil MK, Nadagouda MN, Dionysiou DD (2019) Hydrothermal synthesis of photoactive nitrogen- and boron- codoped TiO<sub>2</sub> nanoparticles for the treatment of bisphenol A in wastewater: synthesis, photocatalytic activity, degradation byproducts and reaction pathways. *Appl Catal B Environ* 241:598–611. <https://doi.org/10.1016/j.apcatb.2018.09.039>
- [29] Liu P, Liu Y, Ye W, Ma J, Gao D (2016) Flower-like N-doped MoS<sub>2</sub> for photocatalytic degradation of RhB by visible light irradiation. *Nanotechnology* 27:225403. <https://doi.org/10.1088/0957-4484/27/22/225403>
- [30] Jiang G-H, Li X, Wei Z, Jiang T-T, Du X-X, Chen W-X (2015) Effects of N and/or S doping on structure and photocatalytic properties of BiOBr crystals. *Acta Metallurgica Sinica-English Letters* 28:460–466. <https://doi.org/10.1007/s40195-015-0220-1>
- [31] Wang W, Cheng L, Liu W (2014) Biological applications of carbon dots. *Sci China Chem* 57:522–539. <https://doi.org/10.1007/s11426-014-5064-4>
- [32] Shafafi S, Habibi-Yangjeh A, Feizpoor S, Ghosh S, Maiyalagan T (2020) Carbon dots and Bi<sub>4</sub>O<sub>5</sub>Br<sub>2</sub> adhered on TiO<sub>2</sub> nanoparticles: Impressively boosted photocatalytic efficiency for removal of pollutants under visible light. *Sep Purif Technol* 250:117179. <https://doi.org/10.1016/j.seppur.2020.117179>
- [33] Ji M, Zhang Z, Xia J et al (2018) Enhanced photocatalytic performance of carbon quantum dots/BiOBr composite and mechanism investigation. *Chin Chem Lett* 29:805–810. <https://doi.org/10.1016/j.ccl.2018.05.002>
- [34] Wang F, Wang Y, Feng Y et al (2018) Novel ternary photocatalyst of single atom-dispersed silver and carbon quantum dots co-loaded with ultrathin g-C<sub>3</sub>N<sub>4</sub> for broad spectrum photocatalytic degradation of naproxen. *Appl Catal B Environ* 221:510–520. <https://doi.org/10.1016/j.apcatb.2017.09.055>
- [35] Li H, He X, Kang Z et al (2010) Water-soluble fluorescent carbon quantum dots and photocatalyst design. *Angewandte Chemie Int Edn* 49:4430–4434. <https://doi.org/10.1002/anie.200906154>
- [36] Duo F, Wang Y, Fan C, Zhang X, Wang Y (2016) Enhanced visible light photocatalytic activity and stability of CQDs/BiOBr composites: the upconversion effect of CQDs. *J Alloy Compd* 685:34–41. <https://doi.org/10.1016/j.jallcom.2016.05.259>
- [37] Hong Y, Meng Y, Zhang G et al (2016) Facile fabrication of stable metal-free CQDs/g-C<sub>3</sub>N<sub>4</sub> heterojunctions with efficiently enhanced visible-light photocatalytic activity. *Sep Purif Technol* 171:229–237. <https://doi.org/10.1016/j.seppur.2016.07.025>
- [38] Wu K, Song S, Wu H, Guo J, Zhang L (2020) Carbon quantum dots modified Bi<sub>2</sub>WO<sub>6</sub> nanoflowers for enhancing photocatalytic activity: an experimental and DFT study. *Micro Nano Lett* 15:317–322. <https://doi.org/10.1049/mnl.2019.0702>
- [39] Que Q, Xing Y, He Z, Yang Y, Yin X, Que W (2017) Bi<sub>2</sub>O<sub>3</sub>/Carbon quantum dots heterostructured photocatalysts with enhanced photocatalytic activity. *Mater Lett* 209:220–223. <https://doi.org/10.1016/j.matlet.2017.07.115>
- [40] Yi F, Ma J, Lin C et al (2020) Insights into the enhanced adsorption/photocatalysis mechanism of a Bi<sub>4</sub>O<sub>5</sub>Br<sub>2</sub>/g-C<sub>3</sub>N<sub>4</sub> nanosheet. *J Alloy Compd* 821:153557. <https://doi.org/10.1016/j.jallcom.2019.153557>
- [41] Zhao M, Fu Y, Ma H et al (2015) Study of the sulfurized BiO<sub>2</sub>CO<sub>3</sub> as efficient visible-light induced photocatalyst. *J Mater Sci Mater Electron* 26:7882–7888. <https://doi.org/10.1007/s10854-015-3439-8>
- [42] Cheng G, Xiong J, Stadler FJ (2013) Facile template-free and fast refluxing synthesis of 3D desertrose-like BiOCl nanoarchitectures with superior photocatalytic activity. *New J Chem* 37:3207–3213. <https://doi.org/10.1039/c3nj00413a>
- [43] Di J, Xia J, Ji M et al (2015) Carbon quantum dots modified BiOCl ultrathin nanosheets with enhanced molecular oxygen activation ability for broad spectrum photocatalytic properties and mechanism insight. *ACS Appl Mater Interf* 7:20111–20123. <https://doi.org/10.1021/acsami.5b05268>



- [44] Yang S, Chen C, Liu L, Zhu L, Xu X (2017) Facile fabrication of micro-floriated AgBr/Bi<sub>2</sub>O<sub>3</sub> as highly efficient visible-light photocatalyst. *Mater Res Bull* 92:29–38. <https://doi.org/10.1016/j.materresbull.2017.03.055>
- [45] Zhu S, Meng Q, Wang L et al (2013) Highly photoluminescent carbon dots for multicolor patterning, sensors, and bioimaging. *Angewandte Chemie Int Edn* 52:3953–3957. <https://doi.org/10.1002/anie.201300519>
- [46] Feizpoor S, Habibi-Yangjeh A, Ahadzadeh I, Yubuta K (2019) Oxygen-rich TiO<sub>2</sub> decorated with C-Dots: highly efficient visible-light-responsive photocatalysts in degradations of different contaminants. *Adv Powder Technol* 30:1183–1196. <https://doi.org/10.1016/j.apt.2019.03.014>
- [47] Cai T, Liu Y, Wang L et al (2017) Silver phosphate-based Z-Scheme photocatalytic system with superior sunlight photocatalytic activities and anti-photocorrosion performance. *Appl Catal B Environ* 208:1–13. <https://doi.org/10.1016/j.apcatb.2017.02.065>
- [48] Zhang J, Liu Q, Wang J et al (2021) Facile preparation of carbon quantum dots/TiO<sub>2</sub> composites at room temperature with improved visible-light photocatalytic activity. *J Alloy Compd* 869:159389. <https://doi.org/10.1016/j.jallcom.2021.159389>
- [49] Fu S, Yuan W, Liu X et al (2020) A novel 0D/2D WS<sub>2</sub>/BiOBr heterostructure with rich oxygen vacancies for enhanced broad-spectrum photocatalytic performance. *J Colloid Interf Sci* 569:150–163. <https://doi.org/10.1016/j.jcis.2020.02.077>
- [50] Zhao J, Ji M, Di J et al (2017) Synthesis of g-C<sub>3</sub>N<sub>4</sub>/Bi<sub>4</sub>O<sub>5</sub>Br<sub>2</sub> via reactable ionic liquid and its cooperation effect for the enhanced photocatalytic behavior towards ciprofloxacin degradation. *J Photochem Photobiol Chem* 347:168–176. <https://doi.org/10.1016/j.jphotochem.2017.07.023>
- [51] Zhang M, Lai C, Li B et al (2019) Rational design 2D/2D BiOBr/CDs/g-C<sub>3</sub>N<sub>4</sub> Z-scheme heterojunction photocatalyst with carbon dots as solid-state electron mediators for enhanced visible and NIR photocatalytic activity: Kinetics, intermediates, and mechanism insight. *J Catal* 369:469–481. <https://doi.org/10.1016/j.jcat.2018.11.029>
- [52] Chen M, Dai Y, Guo J, Yang H, Liu D, Zhai Y (2019) Solvothermal synthesis of biochar@ZnFe<sub>2</sub>O<sub>4</sub>/BiOBr Z-scheme heterojunction for efficient photocatalytic ciprofloxacin degradation under visible light. *Appl Surf Sci* 493:1361–1367. <https://doi.org/10.1016/j.apsusc.2019.04.160>
- [53] Huang M, Li J, Su W et al (2020) Oriented construction of S-doped, exposed 001 facet BiOBr nanosheets with abundant oxygen vacancies and promoted visible-light-driven photocatalytic performance. *CrystEngComm* 22:7684–7692. <https://doi.org/10.1039/D0CE01187H>
- [54] Tang L, Lv Z-q, Xue Y-c et al (2019) MIL-53(Fe) incorporated in the lamellar BiOBr: promoting the visible-light catalytic capability on the degradation of rhodamine B and carbamazepine. *Chem Eng J* 374:975–982. <https://doi.org/10.1016/j.cej.2019.06.019>
- [55] Zhao C, Liang Y, Li W et al (2017) BiOBr/BiOCl/carbon quantum dot microspheres with superior visible light-driven photocatalysis. *RSC Adv* 7:52614–52620. <https://doi.org/10.1039/C7RA10344A>
- [56] Azami M, Haghghi M, Allahyari S (2018) Sono-precipitation of Ag<sub>2</sub>CrO<sub>4</sub>-C composite enhanced by carbon-based materials (AC, GO, CNT and C<sub>3</sub>N<sub>4</sub>) and its activity in photocatalytic degradation of acid orange 7 in water. *Ultrason Sonochem* 40:505–516. <https://doi.org/10.1016/j.ultsonch.2017.07.043>
- [57] Li YY, He T-Y, Dai R-R et al (2019) Bifunctional gyroidal MOFs: highly efficient Lewis base and Lewis acid catalysts. *Chem Asian J* 14:3682–3687. <https://doi.org/10.1002/asia.201900853>
- [58] Wu K, Song S, Wu H, Guo J, Zhang L (2020) Facile synthesis of Bi<sub>2</sub>WO<sub>6</sub>/C<sub>3</sub>N<sub>4</sub>/Ti<sub>3</sub>C<sub>2</sub> composite as Z-scheme photocatalyst for efficient ciprofloxacin degradation and H<sub>2</sub> production. *Appl Catal A General* 608:117869. <https://doi.org/10.1016/j.apcata.2020.117869>
- [59] Liang Y, Wang X, An W, Li Y, Hu J, Cui W (2019) Ag-C<sub>3</sub>N<sub>4</sub>@ppy-rGO 3D structure hydrogel for efficient photocatalysis. *Appl Surf Sci* 466:666–672. <https://doi.org/10.1016/j.apsusc.2018.10.059>
- [60] Song S, Wu K, Wu H, Guo J, Zhang L (2020) Synthesis of Z-scheme multi-shelled ZnO/AgVO<sub>3</sub> spheres as photocatalysts for the degradation of ciprofloxacin and reduction of chromium(VI). *J Mater Sci* 55:4987–5007.

**Publisher's Note** Springer Nature remains neutral with regard to jurisdictional claims in published maps and institutional affiliations.